Supplementary material
Global surface-ocean pCO_2 and sea-air CO_2 flux variability from an observation-driven ocean mixed-layer scheme

C. Rödenbeck, R. F. Keeling, D. C. E. Bakker, N. Metzl, A. Olsen, C. Sabine, and M. Heimann

S1 Implementation details

S1.1 Auxiliary quantities of gas exchange

The solubility depends on temperature T (in $^\circ$C) and salinity S, parameterized according to Weiss (1974)

$$L = l \cdot \exp\left(A_1 + A_2 \frac{100\mathrm{K}}{T+T_0} + A_3 \ln\frac{T+T_0}{100\mathrm{K}} + \frac{S}{‰}\left\{ B_1 + B_2 \frac{T+T_0}{100\mathrm{K}} + B_3 \left(\frac{T+T_0}{100\mathrm{K}}\right)^2 \right\} \right) \frac{\mathrm{mol}}{\mathrm{kg}\cdot\mathrm{atm}} \tag{S1.1}$$

with species-dependent coefficients from Table S1.1. For CO_2, the additional factor l allows to use this solubility with partial pressure rather than fugacity (temperature dependence neglected); for the other gases it converts from Bunsen solubility.

The atmospheric dry-air pressure is

$$p^{\mathrm{dry}} = p^{\mathrm{baro}} - p^{H_2O} \tag{S1.2}$$

with the correction for water vapor pressure calculated from SST and SSS as (Weiss and Price, 1980)

$$p^{H_2O} = p^{\mathrm{baro}} \cdot \exp\left(24.4543 - 67.4509 \frac{100\mathrm{K}}{T+T_0} - 4.8489 \ln\frac{T+T_0}{100\mathrm{K}} - 0.000544 \frac{S}{‰} \right) \tag{S1.3}$$

The Schmidt number depends on T according to (Wanninkhof (1992) based on data by Jähne et al. (1987))

$$Sc = C_0 + C_1 \left(\frac{T}{^\circ\mathrm{C}}\right) + C_2 \left(\frac{T}{^\circ\mathrm{C}}\right)^2 + C_3 \left(\frac{T}{^\circ\mathrm{C}}\right)^3 \tag{S1.4}$$

with coefficients from Table S1.1 (coefficients are valid for $S = 35‰$, i.e., any salinity dependence is neglected). The reference Schmidt number (arbitrary due to the scaling of Γ in Eq. (A2)) is

$$Sc^{\mathrm{Ref}} = 660 \tag{S1.5}$$

Table S1.1. Coefficients used to calculate solubilities Eq. (S1.1) and Schmidt numbers Eq. (S1.4).

	CO_2	O_2	N_2
l	0.996	$\frac{\mathrm{kg/mol}}{\varrho V_{\mathrm{ideal}}}$	$\frac{\mathrm{kg/mol}}{\varrho V_{\mathrm{ideal}}}$
A_1	-60.2409	-58.3877	-59.6274
A_2	93.4517	85.8079	85.7661
A_3	23.3585	23.8439	24.3696
B_1	0.023517	-0.034892	-0.051580
B_2	-0.023656	0.015568	0.026329
B_3	0.0047036	-0.0019387	-0.0037252
	(Weiss, 1974)	(Weiss, 1970)	
C_0	2073.1	1953.4	2206.1
C_1	-125.62	-128.00	-144.86
C_2	3.6276	3.9918	4.5413
C_3	-0.043219	-0.050091	-0.056988
	(as given in Wanninkhof, 1992)		

S1.2 Numerical solution of the budget equation

For the numerical solution of the budget equation Eq. (A21) with the initial condition Eq. (A22), and the implementation of fixed (a-priori) and adjustable contributions in the inverse estimation, we decompose the DIC concentration

$$\begin{aligned} C_{\mathrm{m}}^{\mathsf{DIC}} &= C_{\mathrm{m}}^{\mathsf{DIC},\mathrm{Ref}} + \Delta C_{\mathrm{m}}^{\mathsf{DIC}} \\ &= C_{\mathrm{m}}^{\mathsf{DIC},\mathrm{Ref}} + \Big(\Delta C_{\mathrm{a}}^{\mathsf{DIC}}(t_{\mathrm{i}}) + \Delta C_{\mathrm{m}}^{\mathsf{DIC},\mathrm{ini}} \Big) + \Delta C_{\mathrm{m}}^{\mathsf{DIC},\mathrm{pri}} + \Delta C_{\mathrm{m}}^{\mathsf{DIC},\mathrm{adj}} \end{aligned} \tag{S1.6}$$

into the temporally constant reference concentration $C_{\mathrm{m}}^{\mathsf{DIC},\mathrm{Ref}}$, an adjustable temporally constant deviation $(\Delta C_{\mathrm{a}}^{\mathsf{DIC}}(t_{\mathrm{i}}) + C_{\mathrm{m}}^{\mathsf{DIC},\mathrm{ini}})$ from the reference determining the initial concentration at the start $t = t_{\mathrm{i}}$ of the inversion period according to Eq. (A22), a fixed deviation $C_{\mathrm{m}}^{\mathsf{DIC},\mathrm{pri}}$ in the absence of interior sources/sinks ($f_{\mathrm{int}}^{\mathsf{DIC}} = 0$) just responding to solubility changes, history and freshwater fluxes, and a deviation $C_{\mathrm{m}}^{\mathsf{DIC},\mathrm{adj}}$ responding to the adjustable ocean-internal fluxes $f_{\mathrm{int}}^{\mathsf{DIC}}$ and to $\Delta C_{\mathrm{m}}^{\mathsf{DIC},\mathrm{ini}}$. Correspondingly, Eq. (A21) decomposes into

$$\frac{\mathrm{d}}{\mathrm{d}t} C_{\mathrm{m}}^{\mathsf{DIC},\mathrm{Ref}} = 0, \qquad \frac{\mathrm{d}}{\mathrm{d}t} \Delta C_{\mathrm{m}}^{\mathsf{DIC},\mathrm{ini}} = 0 \tag{S1.7}$$

$$\begin{aligned} \frac{\mathrm{d}}{\mathrm{d}t} \Delta C_{\mathrm{m}}^{\mathsf{DIC},\mathrm{pri}} &= -\frac{k^{\mathsf{DIC}}}{h} \Delta C_{\mathrm{m}}^{\mathsf{DIC},\mathrm{pri}} \\ &\quad + \frac{k^{\mathsf{DIC}}}{h} \Big(\Delta C_{\mathrm{a}}^{\mathsf{DIC}} - \Delta C_{\mathrm{a}}^{\mathsf{DIC}}(t_{\mathrm{i}}) \Big) + \frac{1}{h\varrho} f_{\mathrm{hist}}^{\mathsf{DIC}} \{ C_{\mathrm{m}}^{\mathsf{DIC},\mathrm{clim}} \} + \frac{1}{h\varrho} f_{\mathrm{frw}}^{\mathsf{DIC}} \end{aligned} \tag{S1.8}$$

$$\begin{aligned} \frac{\mathrm{d}}{\mathrm{d}t} \Delta C_{\mathrm{m}}^{\mathsf{DIC},\mathrm{adj}} &= -\frac{k^{\mathsf{DIC}}}{h} \Delta C_{\mathrm{m}}^{\mathsf{DIC},\mathrm{adj}} \\ &\quad - \frac{k^{\mathsf{DIC}}}{h} \Delta C_{\mathrm{m}}^{\mathsf{DIC},\mathrm{ini}} + \frac{1}{h\varrho} f_{\mathrm{int}}^{\mathsf{DIC}} \end{aligned} \tag{S1.9}$$

Eqs. (S1.8) and (S1.9) are solved with zero initial condition at $t = t_{\mathrm{i}}$. Note that $\Delta C_{\mathrm{m}}^{\mathsf{DIC}}$ will approach a well-defined solution even for any initial condition after some spin-up time because the coefficient $-k^{\mathsf{DIC}}/h$ is negative. Through adjustments to $\Delta C_{\mathrm{m}}^{\mathsf{DIC},\mathrm{ini}}$, a spurious spin-up transient in $\Delta C_{\mathrm{m}}^{\mathsf{DIC}}$ can be avoided. As there are not many data points in the first part of the inversion period, $\Delta C_{\mathrm{m}}^{\mathsf{DIC},\mathrm{ini}}$ is not actually well constrained, but the problem seems small because it only affects the first few months, which are excluded from the mean seasonal cycle.

A small approximation has been employed in the implementation of the history flux. As the history flux depends on the entire time series of $C_{\mathrm{m}}^{\mathsf{DIC}}$, not just the instantaneous concentration, exact treatment would require to include the history flux according to Eq. (A20) into the numerical solver of the differential equation. To avoid that, we always calculate $f_{\mathrm{hist}}^{\mathsf{DIC}}$ from seasonal DIC concentrations $C_{\mathrm{m}}^{\mathsf{DIC},\mathrm{clim}}$ inferred from the $p^{\mathsf{CO_2}}$ climatology (Takahashi et al., 2009)[7], as already indicated in Eq. (S1.8). This leads to some small imbalance in the prior, which however is compensated in the posterior by small spurious offsets in the estimated internal flux, such that the estimated $p_{\mathrm{m}}^{\mathsf{CO_2}}$ and $f_{\mathrm{ma}}^{\mathsf{CO_2}}$ are hardly affected. This as been confirmed numerically by a test run where the history flux has been calculated from the a-posteriori $C_{\mathrm{m}}^{\mathsf{DIC}}$ field of run **SFC** rather than the climatology. Where the internal flux itself is needed (here in the calculation of the $\mathsf{PO_4}$ concentration, Appendix C), the approximation is corrected "after the fact" by re-calculating $f_{\mathrm{int}}^{\mathsf{DIC}}$ from the estimated $C_{\mathrm{m}}^{\mathsf{DIC}}$ field via the budget equation including the correct history flux $f_{\mathrm{hist}}^{\mathsf{DIC}}\{C_{\mathrm{m}}^{\mathsf{DIC}}\}$.

S1.3 Treatment of ice-covered areas

Sea-air gas exchange is very different in ice-covered areas. While sea ice prevents sea-air exchange as considered above, there are carbon fluxes through cracks (leads), gas bubbles and fresh-water dilution from melting ice, etc. (e.g., Takahashi et al. (2009) account for this by reducing sea-air exchange in ice-covered areas to 10% of the open-ocean fluxes, rather than zero fluxes.) As further second-order effects, the ice smoothes the wave field and thus affects gas exchange; large temperature gradients in the overlying atmosphere affect the local sub-grid scale atmospheric circulations; the transport model clearly cannot resolve the atmospheric Arctic boundary layer and may have numerical distortions close to the poles.

[7] The DIC concentration corresponding to the Takahashi et al. (2009) climatology $p_{\mathrm{m}}^{\mathsf{CO_2},\mathrm{clim}}$ has been calculated by inverting Eq. (A10),

$$C_{\mathrm{m}}^{\mathsf{DIC},\mathrm{clim}} = C_{\mathrm{m}}^{\mathsf{DIC},\mathrm{Ref}} + \left(\frac{\partial p_{\mathrm{m}}^{\mathsf{CO_2}}}{\partial C_{\mathrm{m}}^{\mathsf{DIC}}} \right)^{-1} \left[\frac{p_{\mathrm{m}}^{\mathsf{CO_2},\mathrm{clim}}}{\beta(T,T^{\mathrm{Ref}})} - p_{\mathrm{m}}^{\mathsf{CO_2},\mathrm{Ref}} - \frac{\partial p_{\mathrm{m}}^{\mathsf{CO_2}}}{\partial A} \Delta A - \frac{\partial p_{\mathrm{m}}^{\mathsf{CO_2}}}{\partial S} \Delta S \right] \tag{S1.10}$$

An additional practical problem is that many of our driving fields (MLD, buffer factor, mean DIC, etc.) are not available at high northern latitudes. On the other hand, however, the contribution of sea-air fluxes from ice-covered regions is small in the global context.

As a pragmatic solution, we therefore

- scale all piston velocities by a factor related to the instantaneous ice-free fraction,

$$0.9 \cdot \varepsilon + 0.1 \tag{S1.11}$$

- missing driving fields are extrapolated from data-covered regions towards the poles;
- declare all pixels where time-mean ice-free area is less than 50% as inactive; in these regions, ocean quantities are not adjusted in the inversion, but kept at their a-priori values calculated from Takahashi et al. (2009) climatology.

Areas without driving fields also exist along the coasts and in marginal seas. As for the ice-covered areas, fields are extrapolated from open-ocean areas towards West or East, respectively.

S2 Sensitivity cases

In addition to the sensitivity cases mentioned in Sect. 3.3 shown as grey band in Figure 7, various other tests have been performed. Unless mentioned otherwise, their sensitivity is very low (ie., they change the fitted pCO2 field by an amount negligible compared to the grey band).

- Increasing the **a-priori uncertainty** by a factor 2, or decreasing it by a factor 2 (part of grey sensitivity band).
- Increasing the **a-priori spatial correlation length** by a factor 3 (part of grey sensitivity band).
- Changing the **atmospheric CO_2 concentration for the gas exchange** (X^{CO_2}). This was done by (1) performing a fit to the atmospheric CO_2 data using the result of run **SFC** as fixed ocean fluxes (2) creating X^{CO_2} by a forward transport model run from the resulting a-posteriori fluxes, (3) repeating run **SFC** using this X^{CO_2} field. Actually, this procedure could be repeated ("outer loop") to ensure that X^{CO_2} is consistent with the flux estimates, however the sensitivity of the results to X^{CO_2} is low anyway.
- Changing the amplitude of the **seasonally varying mixed-layer depth** h by factor 2 or 1/2 (part of grey sensitivity band). Contrary to what may be expected, the sensitivity of p^{CO_2} is very low; the sensitivity of $f_{\rm int}^{DIC}$ is larger, mainly because the history flux changes; however the sensitivity of the PO_4 field is very low again because the history flux vanishes for both DIC and PO_4.

  This low sensitivity to the seasonality of mixed-layer depth indicates that its missing interannual variations should not be a large problem for applications of the diagnostic scheme to IAV.
- Increasing or decreasing the **gas exchange** (scaling Γ) to the lower or upper end of the range given by Naegler (2009) (part of grey sensitivity band). The sensitivity of p^{CO_2} is low (it does exist because the time constant of the budget equation changes), but higher for the sea-air fluxes which are scaled roughly proportionally to Γ.
- Omitting certain processes in the carbonate chemistry and DIC budget (**alkalinity dependence, salinity dependence, freshwater dilution effect**). There is little change to the estimated p^{CO_2} field, but the ocean-internal fluxes, and thus the PO_4 field, change more strongly. Of course, omitting these processes is expected to deteriorate the result, but the test demonstrates that PO_4 is sensitive to errors in the respective parameterization and its input driving fields (A, S, T) which are hard to quantify.
- Skipping SOCAT data values from all pixels where the first and the last existing measurement are within less than 1 year. Sensitivity very low in most regions, except for North Pacific (where the result is more close to the LDEO-based result of Figure S6.1), the temperate North Atlantic due to the missing Mediterranean values, and the Tropical Indian.
- Skipping **coastal values** in the SOCAT data set (e.g., all values from locations shallower than $400\mathrm{m}$), or also including values less than $200\mu\mathrm{atm}$ or larger than $600\mu\mathrm{atm}$ (normally skipped, Table 1); (sensitivity very low).
- Transferring the SOCAT data values from their **local sea surface temperature** (as given in the data set) to that of its grid cell in our T field, i.e., to the value that should have been measured if T was true. The sensitivity is low, except for the Tropical Atlantic.
- **Data density weighting** of the SOCAT data, similar to that of the atmospheric data (Rödenbeck, 2005). The weighting was done such that averages over months and $\approx 150\mathrm{km}$ areas have similar weight in the cost function (sensitivity very low).
- Omitting the **fugacity factor** in the data (sensitivity very low).

S3 The history flux

Here we show analytically that the history flux $f_{\rm hist}$ according to Eq. (A20) compensates long-term imbalances of the carbon budget Eq. (A18) arising from covariance between carbon concentration C and mixed-layer depth h ("seasonal rectification").

Consider the mixed-layer concentration of any tracer, e.g. $C = C_{\rm m}^{\rm DIC}$. Summarizing all fluxes other than the history flux into f, the budget equation Eq. (A18) is

$$\frac{{\rm d}C}{{\rm d}t} = \frac{1}{h\varrho}\,(f + f_{\rm hist}) \tag{S3.1}$$

The history flux had been defined as (Eq. (A20))

$$f_{\rm hist}(t) = \varrho \cdot \Big(C(t_{\rm prev}) - C(t) \Big) \cdot \Theta\left(\frac{{\rm d}h}{{\rm d}t} \right) \tag{S3.2}$$

with $t_{\rm prev} = t_{\rm prev}(t)$ giving the previous time when the mixed layer was as deep as at t, i.e.,

$$h(t_{\rm prev}(t)) = h(t) \tag{S3.3}$$

From the mixed-layer concentration C (tracer amount per unit water mass) we consider the total tracer amount in the mixed layer column (amount per ocean surface area),

$$M = \varrho h \cdot C \tag{S3.4}$$

Its time-rate of change is

$$\frac{{\rm d}M}{{\rm d}t} = \varrho h \cdot \frac{{\rm d}C}{{\rm d}t} + C \cdot \varrho \frac{{\rm d}h}{{\rm d}t} \tag{S3.5}$$

We consider a time period starting at a time t_- when the mixed layer is at a depth $h_{\rm d}$, then shoals until reaching a minimum depth $h_{\rm s}$ at an intermediate time t_0, and then deepens until again reaching depth $h_{\rm d}$ at time t_+. During shoaling ($t_- \le t \le t_0$), the total tracer amount changes as

$$\frac{{\rm d}M}{{\rm d}t} = f(t) + C(t) \cdot \varrho \frac{{\rm d}h}{{\rm d}t} \tag{S3.6}$$

(substituting Eqs. (S3.1) and (S3.2) into Eq. (S3.5), and considering that the history flux is zero during shoaling). During deepening ($t_0 \le t \le t_+$), we have

$$\frac{{\rm d}M}{{\rm d}t} = f(t) + C(t_{\rm prev}(t)) \cdot \varrho \frac{{\rm d}h}{{\rm d}t} \tag{S3.7}$$

The cumulative changes in tracer during shoaling and deepening, respectively, are then

$$\begin{aligned} M(t_0) - M(t_-) &= \int_{t_-}^{t_0} f(t){\rm d}t \; + \overbrace{\int_{t_-}^{t_0} C(t) \cdot \varrho \frac{{\rm d}h}{{\rm d}t}{\rm d}t}^{\int_{h_{\rm d}}^{h_{\rm s}} C(t(h)) \cdot \varrho {\rm d}h} \\ M(t_+) - M(t_0) &= \int_{t_0}^{t_+} f(t){\rm d}t + \underbrace{\int_{t_0}^{t_+} C(t_{\rm prev}(t)) \cdot \varrho \frac{{\rm d}h}{{\rm d}t}{\rm d}t}_{\int_{h_{\rm s}}^{h_{\rm d}} C(t_{\rm prev}(h)) \cdot \varrho {\rm d}h} \end{aligned} \tag{S3.8}$$

At the braces above/below the second integrals, the independent integration variable has been transformed from t to h, which is possible because $h(t)$ is bijective within each part of the considered time interval. The new form reveals that the two integrants are in fact equal: $t(h)$ in the upper line (during shoaling) is identical to $t_{\rm prev}(h)$ in the lower line. The integrals however have opposite sign because the integration limits are interchanged. Therefore, they cancel on summing both lines of Eq. (S3.8), giving

$$M(t_+) - M(t_-) = \int_{t_-}^{t_+} f(t){\rm d}t \tag{S3.9}$$

Thus the total change in tracer amount during the considered time period only depends on the fluxes f, while the covariance effects have been cancelled by the history flux: Without the history flux, the lower line of Eq. (S3.8) would not involve $C(t_{\mathrm{prev}})$ but $C(t)$ from the time interval after t_0, which is in general different from $C(t)$ before t_0, leading to a spurious net effect of considerable size.

The h climatology used here represents an unimodal cycle of shoaling and deepening; thus the argumentation applies directly. If the mixed-layer is shoaling and deepening multiple times, the yearly cycle needs to be subdivided into several shoaling/deepening periods that can be suitably paired according to the relation of t during deepening and the corresponding $t_{\mathrm{prev}}(t)$ during shoaling.

S4 Testing the retrieval capacity of the atmospheric data (for run ATM)

Analogously to Appendix B, we tested the ability of the atmospheric data at the available measurement sites to constrain p^{CO_2} (or flux) seasonality: Synthetic atmospheric data were generated by a forward run of the atmospheric transport model using fluxes calculated from the Takahashi et al. (2009) climatology (plus fossil fuel emissions and land exchange as in the prior, i.e., no seasonality over land). The comparison between the fit to these synthetic data and the known "truth" was not only done in terms of p^{CO_2} but also in terms of land-air and sea-air fluxes.

The model is largely able to retrieve region-to-region differences of the known "truth" from the atmospheric information (Figure S4.1). In some regions (e.g., North Pacific) the fit is only good in the run with the least tight prior. In other regions (e.g., the South temperate regions), in contrast, more tight priors are needed to damp spurious signals. The sensitivity to the prior tightness indicates that the fit to (synthetic) atmospheric data is less robust, compared to the fit to p^{CO_2} data. However, in a changed system where the land-atmosphere exchange is fixed (i.e., no adjustable degrees of freedom over land, such that the land fluxes already coincide with the "truth"), this sensitivity becomes much smaller (not shown), indicating that the limited robustness is to large part related to shifts of signals between land and ocean. Consistently, synthetic runs with less tight priors (but original system) also show less spurious variability attributed to land fluxes (not shown).

To investigate this land-ocean crosstalk further, a complementary synthetic run was performed, using a different "truth" having zero (constant) ocean-atmosphere fluxes but seasonal land fluxes (taken from the BiomeBGC biosphere model, which is similar in seasonality to the normal atmospheric CO_2 inversion estimates). As expected, the fit to the synthetic data calculated from this "truth" leads to spurious variability also over the ocean (not shown). Though the amplitude of this spurious ocean variability is comparable to the range from the sensitivity to prior tightness (confirming the paragraph above), it is considerably smaller than the signals themselves (e.g., according to run **SFC**), indicating that the density of the atmospheric station network is actually sufficient to separate land and ocean. In particular, the error amplitude is much smaller than the difference between the p^{CO_2}-based (**SFC**) and atmosphere-based (**ATM**) results, especially in the region of the largest discrepancy (North Pacific). Thus this discrepancy cannot be explained by land-ocean crosstalk from limited information in the atmospheric data.

However, land-ocean crosstalk can also arise from errors of the modelled atmospheric transport: If some site is influenced by land signals in reality, but by ocean signals in the model, the inversion will try to match the data from this station by wrongly adjusting ocean rather than land fluxes. Support of this assumption comes from the fact that the discrepancy in the North Pacific is larger when using the coarser-resolution transport model whose errors are likely larger.[8]

[8]We considered whether the suite of TransCom-3L3 inversion results (done by various groups using different transport models but also different inversion methodologies) could be used to reveal such transport model errors. TransCom-3L3 results comprise largely different seasonal cycles, also in the North Pacific. Conclusions from this inter-comparison on possible model errors are difficult, however, also because some of the inversions use the Takahashi et al. (2009) climatology already as Bayesian prior.

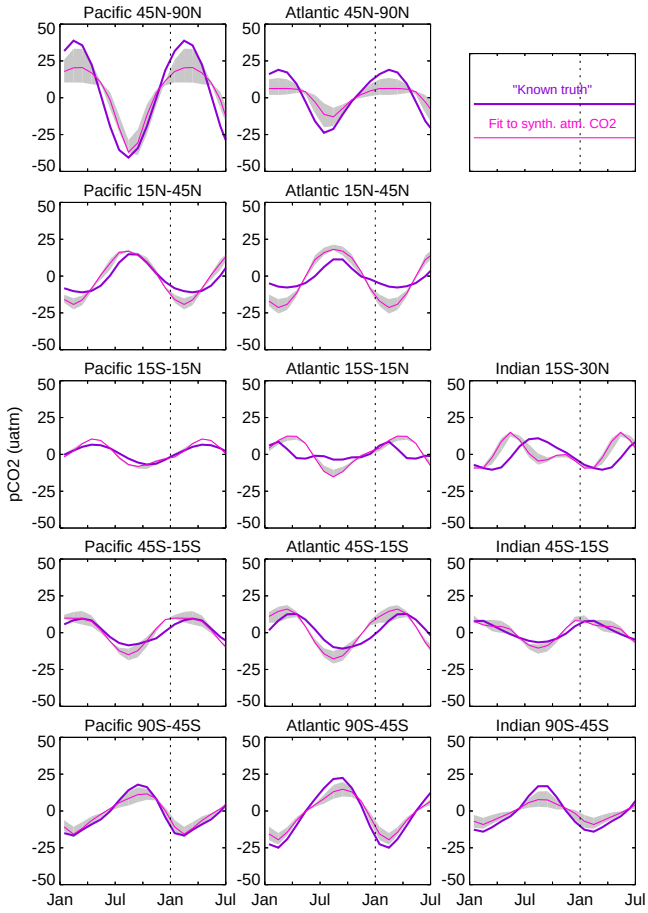

Fig. S4.1. Fit of the diagnostic scheme to synthetic atmospheric CO_2 data, created from a forward run of the atmospheric transport model using sea-air fluxes calculated from the Takahashi et al. (2009) climatology and fluxes identical to the prior on land (constant Net Ecosystem Exchange plus fossil fuel emissions). For computational efficiency, a coarser version of the transport model has been used (for both forward run and inversion). The grey band gives the sensitivity to the strength of the Bayesian prior, with looser priors leading to closer match of the "known truth".

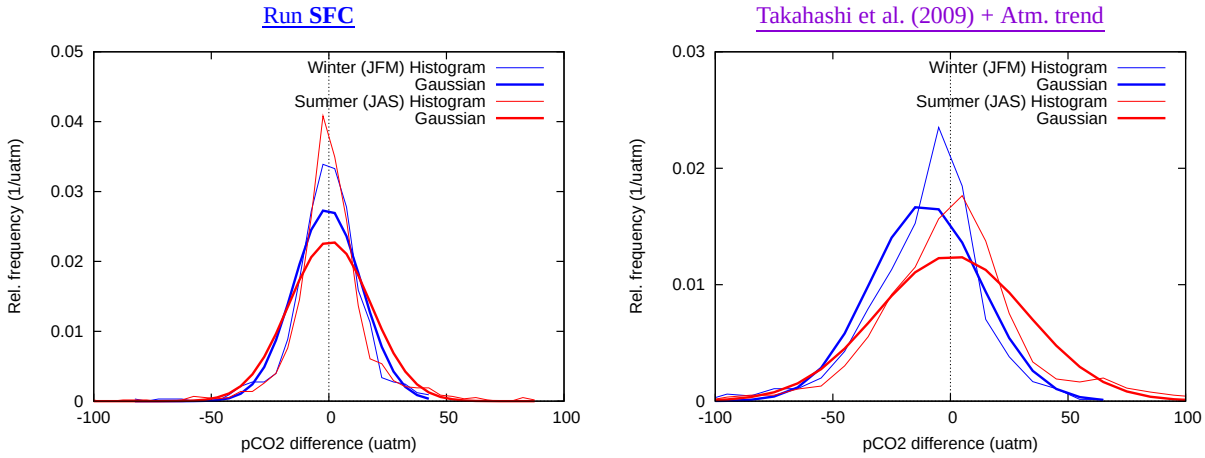

Fig. S5.1. Histograms of p^{CO_2} residuals (μatm, horizontal axis) against SOCAT data. Left and right columns refer to the two cases shown in Figure 7. Thin lines show the relative abundance (within bins of $5\mu atm$ or $10\mu atm$, respectively) of differences between the respective field and the SOCAT value over all pixels from the North Pacific (North of 45° N) and all time steps where data exist and which lie either in winter (Jan-Feb-Mar, blue) on summer (Jul-Aug-Sep, red). Respective thick lines give a Gaussian of the same mean and standard deviation. See Supplementary material, Figure S5.2 for maps of seasonal residuals.

S5 Residuals

Figure 8 and Figure 10 already illustrated how the diagnostic model fits the SOCAT data at example locations. To more systematically judge the success of the fit and investigate the differences of the results to the Takahashi et al. (2009) climatology (Figure 7), we look at the differences of the estimated p^{CO_2} fields and the data at those locations/times where SOCAT data points exist. Figure S5.1 (left, repeating Figure 9) gives histograms of these residuals within the North Pacific region as example (where differences between the two methods in Figure 7 are largest). The mean of these residuals is close to zero. The distribution is symmetric as required mathematically, though it has wider tails than the Gaussian assumed in Bayesian estimation theory. There is very small seasonal bias between winter and summer. From a similar calculation, Figure S5.1 (right) shows the difference between Takahashi et al. (2009) (monthly climatology plus the atmospheric trend from $p_a^{CO_2}$, Eq. (A3)) and the SOCAT data points. The climatology is smaller in winter by about $10\mu atm$ than SOCAT, consistent with the difference to the SOCAT-based fit (Figure 7, upper left panel).

A spatial picture of the biases is given in Figure S5.2. In most areas, mean residuals of the fit in run **SFC** (top left panel) are within $\pm 3\mu atm$ (grey pixels). The seasonal bias (shown as the differences between the residuals restricted to (northern) summer (Jul-Aug-Sep) minus winter (Jan-Feb-Mar) where both averages exist) is mostly small as well or scattered in both directions. Differences between the Takahashi et al. (2009) climatology and SOCAT values in mean and seasonal amplitude (bottom panels) are more systematic in some regions, especially the high Northern areas, as well as the tropical and South Pacific. The comparison is consistent with the differences between the mapping methods seen in Figure 7. However, part of these larger residuals are just due to the fact that there are no interannual variations in the Takahashi et al. (2009) climatology, except for the rising trend in parallel to the atmosphere added by us for this comparison. For a more fair comparison, we thus also considered a case where the interannual variations contained in our results have been replaced by the same rising trend (middle panels). The fact that this leads to larger values of mean residual and seasonal bias than the original run **SFC** reflects that different seasons have been sampled in different years. On the one hand, this limits the informative value of the metrics of Figure S5.2. On the other hand, the unequal data distribution may also lead to spurious interannual variations in our estimates themselves. Nevertheless, the performance of the degraded run **SFC** is still somewhat better than the climatology also in data-dense regions like the North Atlantic where such sampling artifacts may be expected to be less important. Thus we take the comparison of seasonal biases as a tentative confirmation of the $p_m^{CO_2}$ seasonal cycles in run **SFC** being slightly larger in several regions than those estimated by Takahashi et al. (2009).

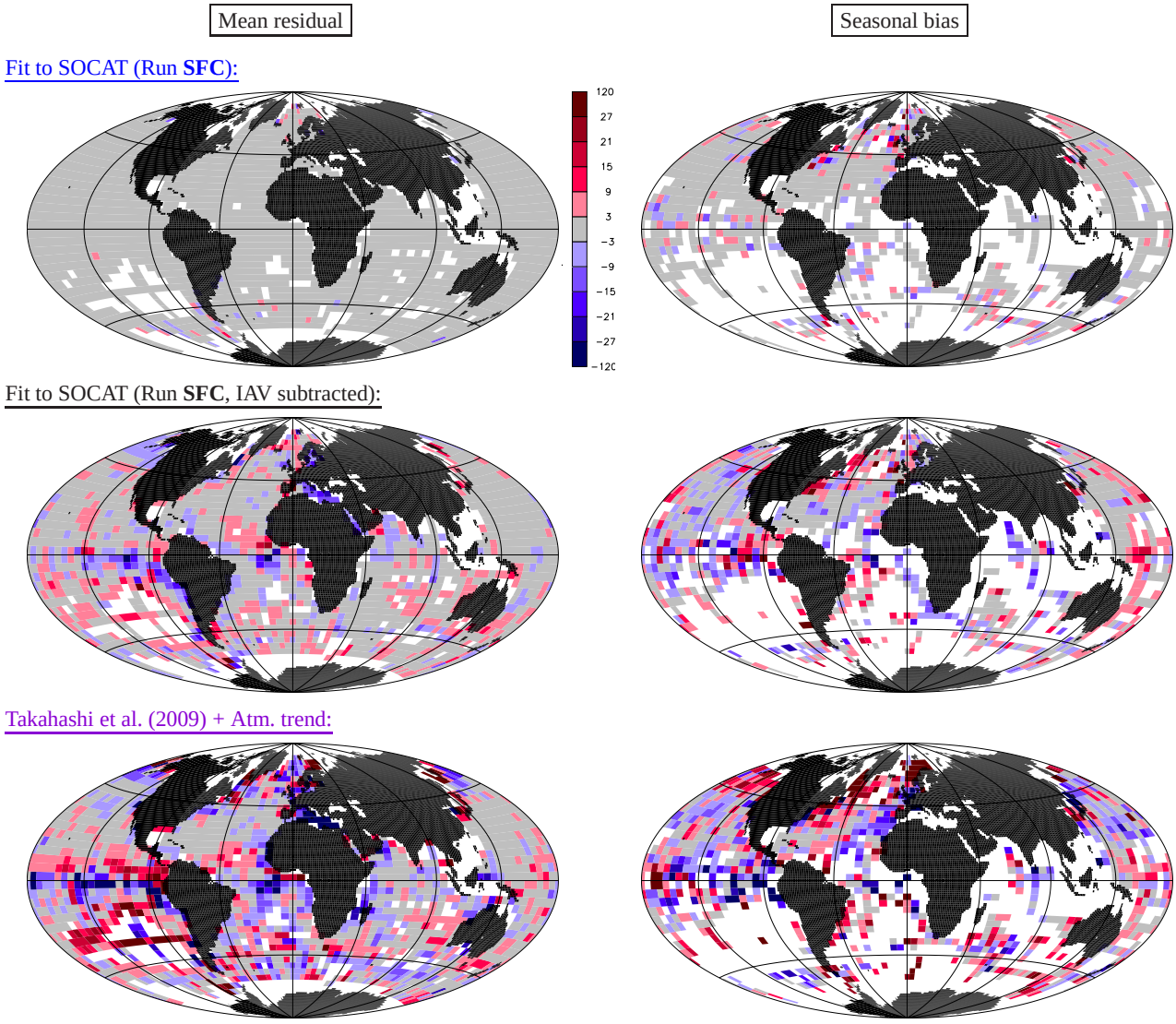

Fig. S5.2. Maps of p^{CO_2} residuals (μatm) of run **SFC** against SOCAT data (top), and difference between the Takahashi et al. (2009) climatology (supplemented by a rising trend in parallel to the atmosphere to avoid unduly large residuals in years away from 2000) and the SOCAT data (bottom). For a fair comparison, residuals are also shown for a degraded run **SFC** where the estimated interannual variations have been replaced by the atmospheric rise (middle). For each pixel, the difference between the respective field and the SOCAT value is shown, averaged over all time steps where data exist (left panels). The seasonal bias in the residuals is shown as the differences between the residuals restricted to (northern) summer (Jul-Aug-Sep) minus winter (Jan-Feb-Mar). White areas do not have SOCAT data within the considered averaging periods. (Note that the calculation is done on TM3 grid, i.e., SOCAT values have been averaged over pixels and daily time steps as used in the fit, and Takahashi et al. (2009) has been grid-converted, which may slightly exaggerate the mismatch for the Takahashi et al. (2009) climatology.)

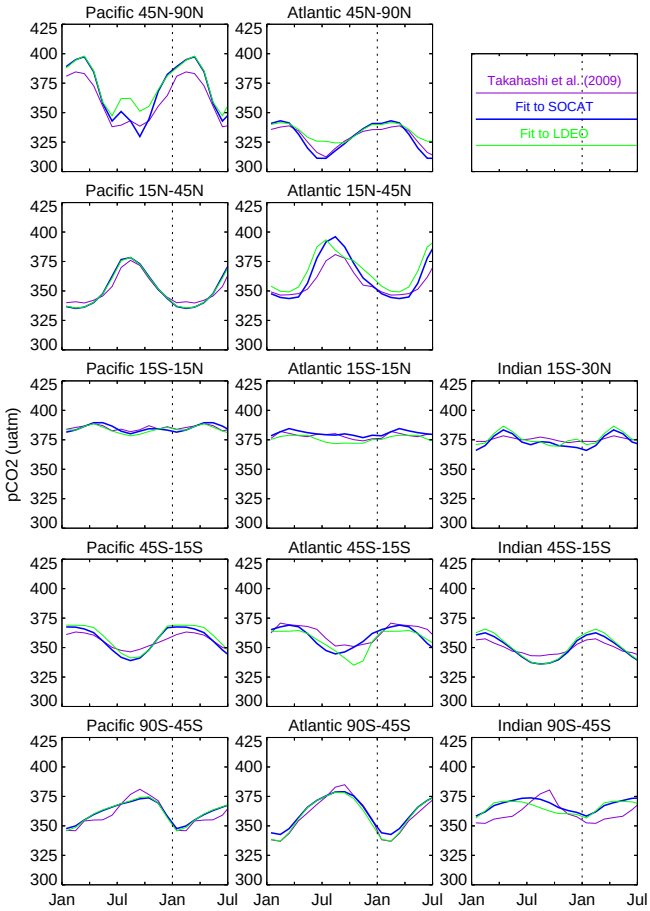

Fig. S6.1. Seasonality of p^{CO_2} as Figure 7, additionally compared to the fit of the diagnostic scheme to LDEO data (Takahashi et al., 2010).

S6 Fit to the LDEO data base

Partly, the differences between our results and the Takahashi et al. (2009) climatology (Figure 7) can be traced to the fact that the climatology is based on a different set of data points (the LDEO data set, Takahashi et al., 2010): When fitting the diagnostic scheme to p^{CO_2} values from the LDEO data base rather than to SOCAT, the results get closer to the climatology in many regions (Figure S6.1), e.g., in the North Pacific where Figure 7 revealed largest differences. Note that the set of LDEO data points used in the fit here is not exactly the same as that used in the Takahashi et al. (2009) climatology, because our fit can only use the data from the inversion period and because the Takahashi et al. (2009) climatology excludes El Niño and coastal values.

There is differences between the fit of the diagnostic scheme to SOCAT or LDEO also in other regions. Most of these (e.g., in the temperate South Atlantic) arise because the data density in LDEO is smaller than in SOCAT: Synthetic-data tests analogous to Figure 14 reveal that LDEO's density gives a weaker constraint on p^{CO_2} seasonality there (not shown).

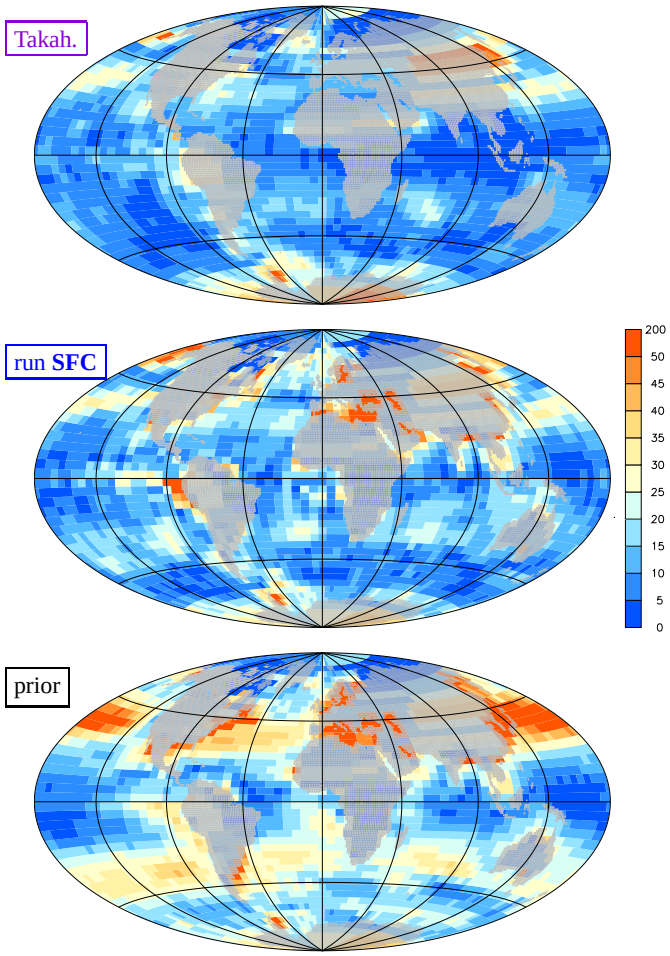

Fig. S7.1. Amplitude of the mean seasonal cycle of surface-ocean CO_2 partial pressure (μatm, identical color scale). Top: Takahashi et al. (2009) (regridded and extrapolated towards the coasts and marginal seas); middle: as estimated by fitting the diagnostic scheme to the SOCAT data (run **SFC**, as Figure 4); bottom: prior. The amplitude is given as temporal standard deviation of the monthly mean $p_{\mathrm{m}}^{\mathrm{CO_2}}$ at each pixel.

S7 Additional figures

A number of figures are added here to give background information on specific aspects.

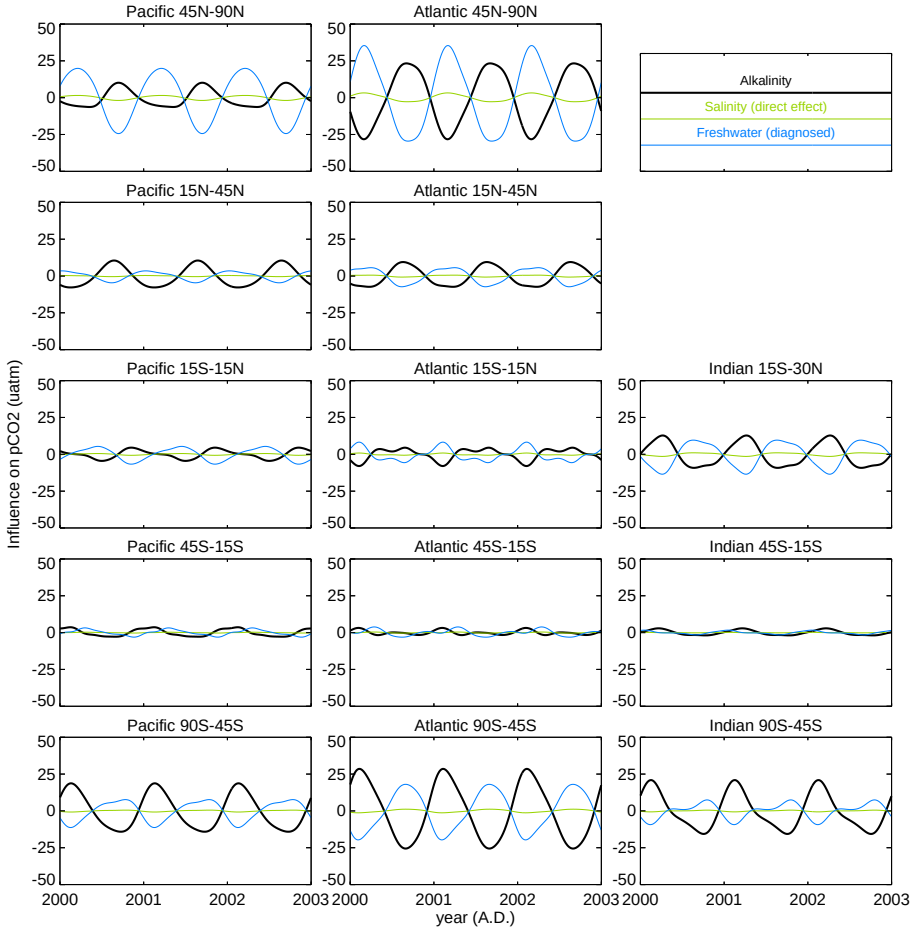

Fig. S7.2. Contributions to the $p_{\mathrm{m}}^{\mathrm{CO_2}}$ seasonality from variations in Alkalinity (black), salinity (direct effect on chemical equilibrium only, green), and freshwater dilution of DIC (calculated in the scheme through $f_{\mathrm{frw}}^{\mathrm{DIC}}$, Eq. (A19), but approximated here by $\frac{\partial p_{\mathrm{m}}^{\mathrm{CO_2}}}{\partial C_{\mathrm{m}}^{\mathrm{DIC}}} \frac{C_{\mathrm{m}}^{\mathrm{DIC,Ref}}}{S^{\mathrm{Ref}}} \left(S - S^{\mathrm{Ref}}\right)$, blue). Three arbitrary years are shown.

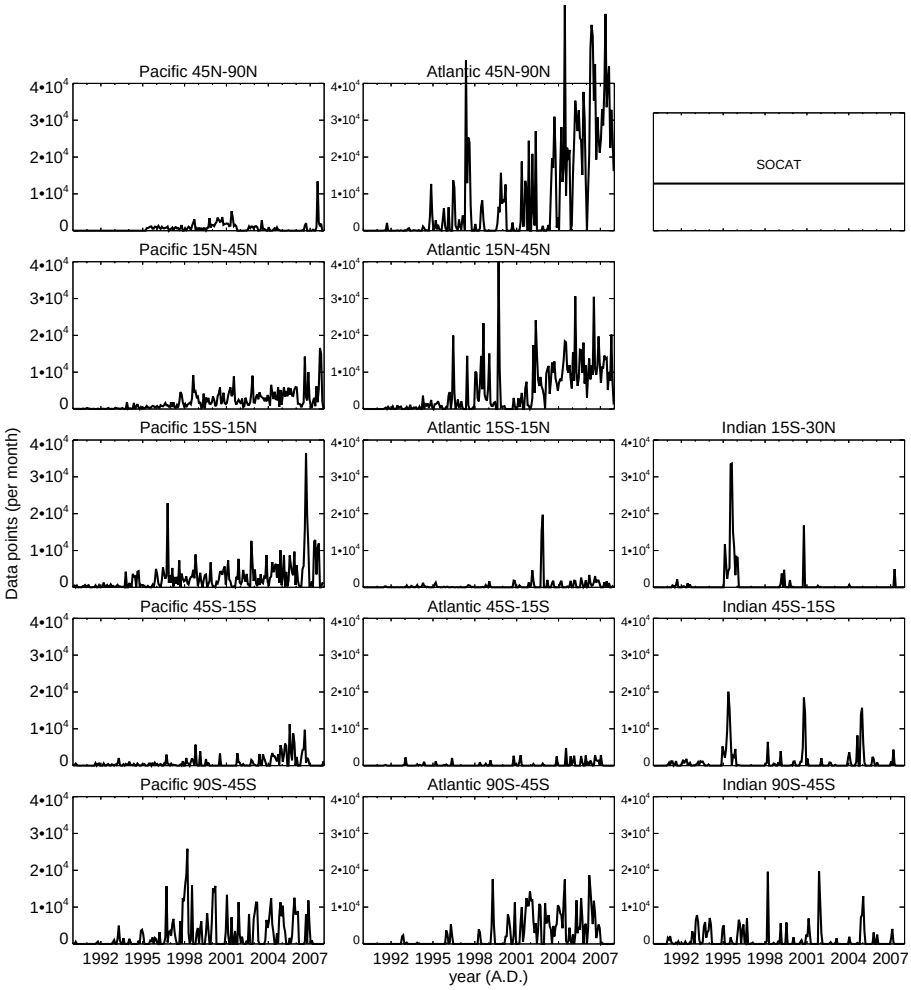

Fig. S7.3. Number of pixels with data points in the SOCAT data base for each month of the calculation. (Off-scale values in the North Atlantic are allowed for the sake of a more readable y scale.)

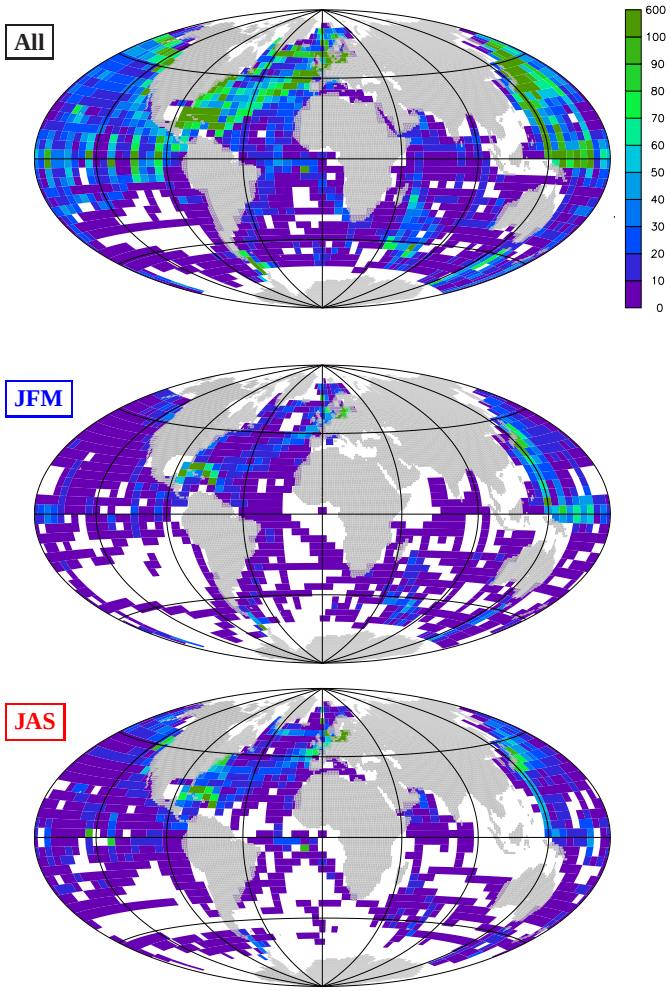

Fig. S7.4. Number of time steps where SOCAT data exist, during all the calculation period (top) or during (northern) winter (JFM, middle) or summer (JAS, bottom). White pixels have no data at all in the respective period.

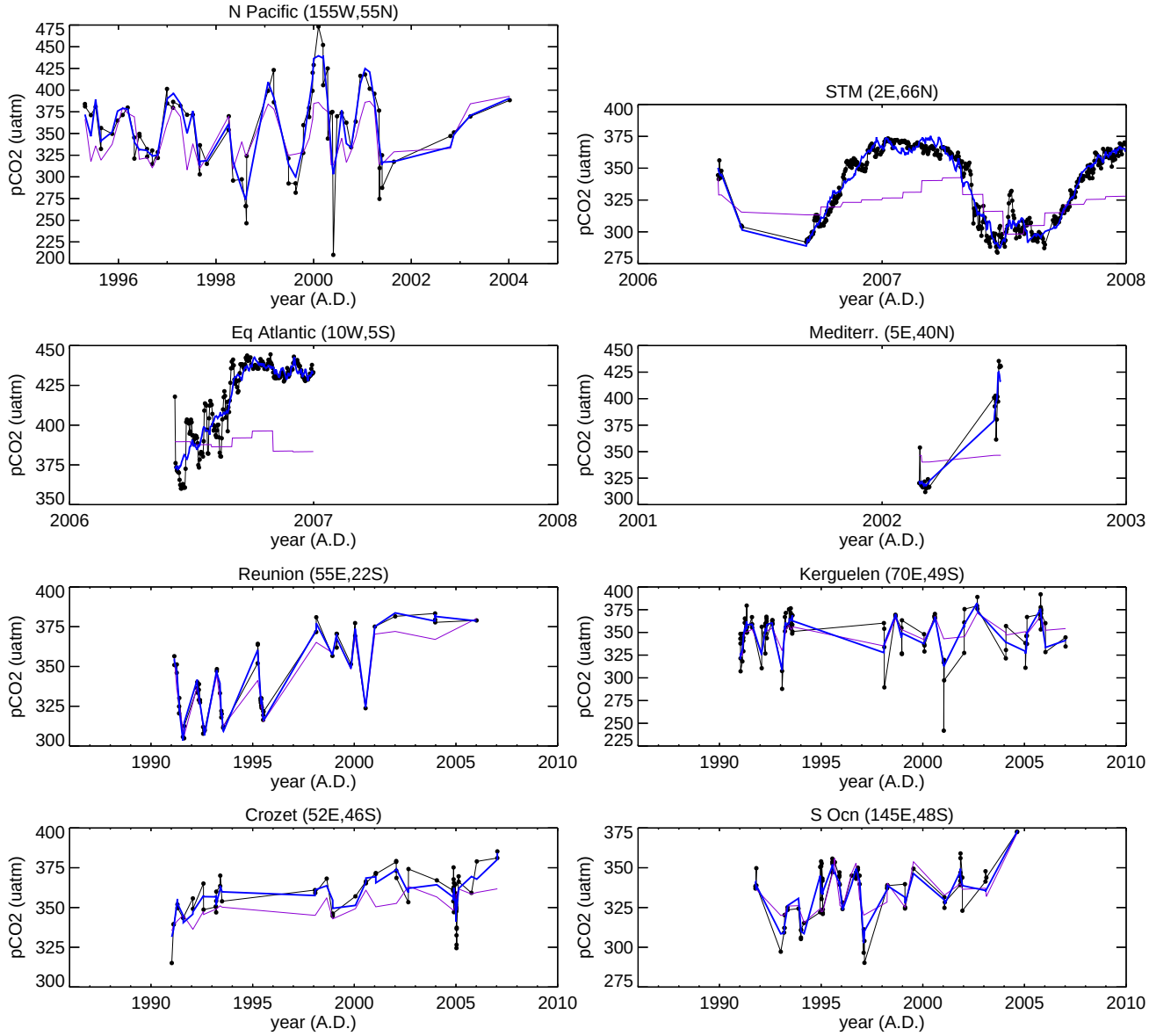

Fig. S7.5. Comparison between the estimated p^{CO_2} field (run **SFC**, blue) and the original SOCAT data (black dots) as Figure 8, for various test locations where SOCAT observations exist over various years or on high frequency. The monthly climatology by Takahashi et al. (2009) (regridded –in the Mediterranean extrapolated from Atlantic open-ocean values– and with added trend parallel to the atmospheric CO_2 increase, violet) is also given. The estimated field and the climatology have been picked at the times where measurements exist (connected by straight lines for clarity); the time axes have been limited to respective years with data.
Example locations shown here have been chosen for having observations either on a high frequency or in many years. The vicinity around Kerguelen Islands may differ from the surrounding large-scale p^{CO_2} field due to large algal blooms occurring almost every year (likely associated to natural fertilization) leading to very low p^{CO_2} during austral summer (Lourantou and Metzl, 2011).

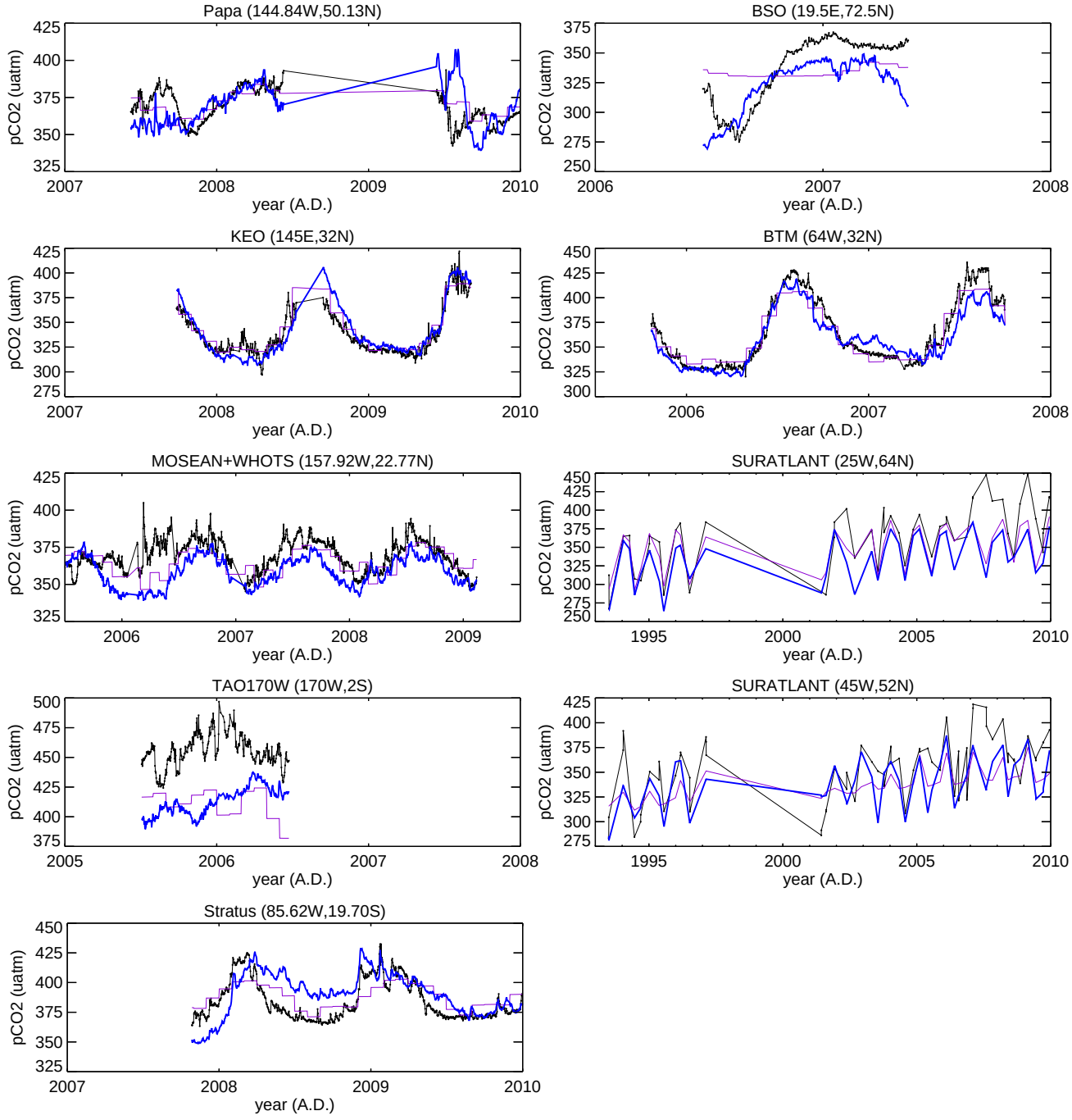

Fig. S7.6. Comparison between the estimated p^{CO_2} field (run **SFC**, blue) and independent p^{CO_2} measurements not in SOCAT v1.5, at various locations in the Pacific (left) or Atlantic (right): BSO – Arthun et al. (2012), SURATLANT – Corbière et al. (2007); Metzl et al. (2010), others – Sabine et al. (2010). The monthly climatology by Takahashi et al. (2009) (regridded and with added trend parallel to the atmospheric CO_2 increase, violet) is also given. The estimated field and the climatology have been picked at the times where measurements exist (connected by straight lines for clarity); the time axes have been limited to respective years with data.

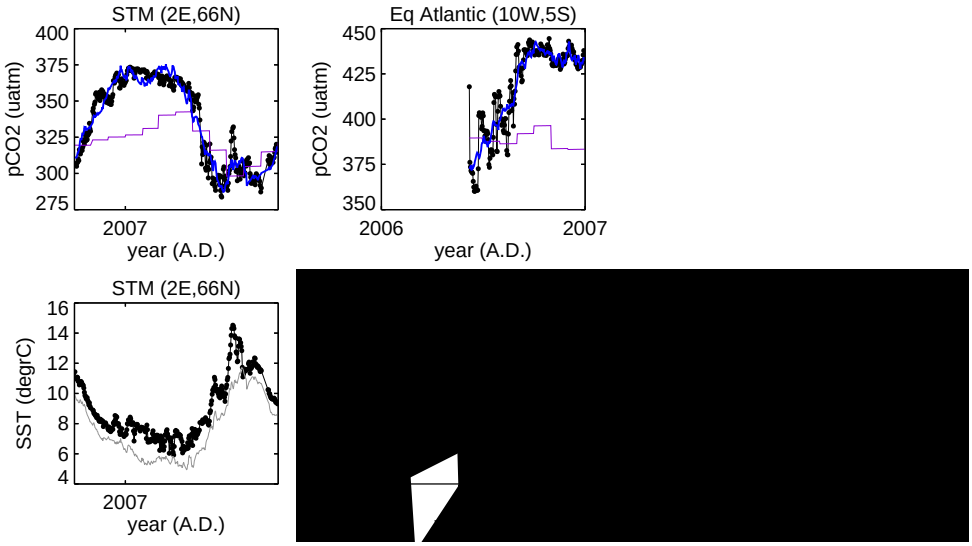
STM (2E,66N)
pCO2 (uatm)
400
375
350
325
300
275
2007
year (A.D.)
Eq Atlantic (10W,5S)
pCO2 (uatm)
450
425
400
375
350
2006
2007
year (A.D.)
STM (2E,66N)
SST (degrC)
16
14
12
10
8
6
4
2007
year (A.D.)